# Morphology-Dependent Trap Formation in Bulk Heterojunction Photodiodes

Guozheng Shao, Glennis E. Rayermann, Eric M. Smith, and David S. Ginger*

Department of Chemistry, University of Washington, Seattle Washington 98195, United States

ⓢ Supporting Information

ABSTRACT: We show that local structural variation affects the rate of aging in nanostructured polymer solar cells by comparing time-resolved electrostatic force microscopy (trEFM) and conventional device measurements on model polymer blends. Specifically, we study photovoltaic devices made from 1:1 blends of the polyfluorene copolymers poly(9,9′-dioctylfluorene-co-bis-N,N′-(4-butylphenyl)-bis-N,N′-phenyl-1,4-phenylene-diamine) (PFB) and poly(9,9′-dioctylfluorene-co-benzothiadiazole) (F8BT). We photooxidize these films in situ using 365, 405, and 455 nm illumination under ambient conditions, with the wavelengths chosen to preferentially excite the different components. During photooxidation, we observe a faster loss of photocurrent generation from F8BT-rich domains, leaving the PFB-rich phases to show higher photoresponse even at wavelengths absorbed predominantly by F8BT. We propose that this effect is due to the more rapid degradation of PFB hole-transport pathways in the F8BT-rich regions, resulting in a loss of percolation pathways for hole transport in the F8BT-rich phase.
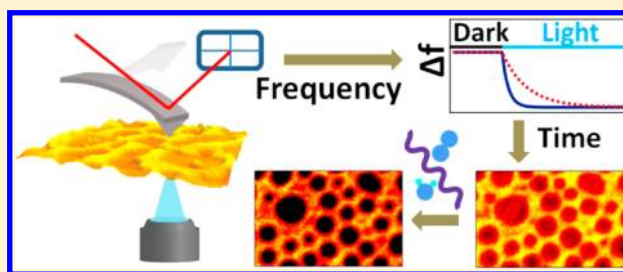
1. INTRODUCTION

Since the first reports of blended polymer heterojunctions,[1,2] the efficiency of organic photovoltaics (OPVs) has improved dramatically, with reports of single-layer devices now approaching 10%[3] and tandem organic solar cells exceeding 10%.[4,5] Over the same time period, scientific interest in these materials has also increased—in part because of the potential to achieve large-area, low-cost solar cells via solution processing of flexible organic semiconductors.[6-9] Nevertheless, a major concern that could limit the widespread use of OPVs is their long-term stability.[10]

Studies have shown that OPV device performance tends to degrade over time because of several causes,[10,11] including chemical interactions at the metal/organic interface,[12] morphological instabilities in the blended active layers,[13] and both reversible and irreversible chemical changes of the semiconductor materials.[14] To some extent, inverted device architectures have mitigated the need for reactive metal cathodes,[15,16] and a variety of cross-linking and other strategies can be used to stabilize polymer film morphologies.[17-19] Suppressing chemical changes in the organic semiconductors is still largely achieved via encapsulation.[10]

Even if OPVs ultimately use some form of encapsulation, a better fundamental understanding of the mechanisms that lead to chemical degradation of active organic semiconductor layers in bulk heterojunction OPVs could still enable better design, synthesis, and processing strategies to achieve more stable OPV devices. Whereas there has been a limited amount of work in this area,[10,11,20] the correlations between local film structure and photooxidation/trap formation in OPVs are essentially unknown. This is unfortunate because heterogeneity is ubiquitous in organic semiconductors,[9,21,22] and one might expect local compositional or structural variations to lead to variations in degradation rates.

Photooxidation of OPVs is often studied by optical methods,[10,23,24] which yield chemical specificity but lack electrical information. Furthermore, optical probes are typically diffraction-limited with resolutions of hundreds of nanometers.[23,24] Electrical scanning probe microscopy methods have the potential to probe local variations in OPV properties such as charge transport, photocurrent collection, and trapping/recombination.[25-30] Indeed, we have previously shown that time-resolved electrostatic force microscopy (trEFM) can be used to characterize local trap formation in conjugated polymer blends.[28] However, in that work, we did not study the spatial variations in photooxidation across a heterogeneous film. Likewise, Sengupta et al. have applied cAFM and SKPM to study photooxidation of polymer blends[31] but focused their studies only on differences between light and dark exposed regions of an OPV film and not on variations in photooxidation across the structurally heterogeneous domains of the bulk heterojunction film.

Here we bridge this critical gap to demonstrate that local composition affects the rate of photooxidation in nanostructured polymer solar cells. We do so by comparing

trEFM with conventional device measurements on blends of the model polymers poly(9,9′-dioctylfluorene-*co*-bis-*N*,*N*′-(4-butylphenyl)-bis-*N*,*N*′-phenyl-1,4-phenylene-diamine) (PFB) and poly(9,9′-dioctylfluorene-*co*-benzothiadiazole) (F8BT).

2. MATERIALS AND METHODS

2.1. Materials and Device Fabrication. PFB (MW = 80 000−120,000, PDI = 2.0) was purchased from American Dye Source (ADS232GE). F8BT (MW = 10 000−20 000, PDI < 3) was purchased from Sigma-Aldrich (product no. 698687). Structures for both materials are shown in Figure 1. Xylene
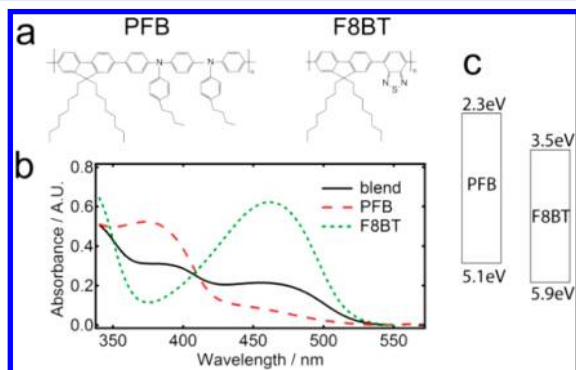

Figure 1. (a) Chemical structures of PFB and F8BT. (b) UV−vis absorbance spectra for our PFB, F8BT, and 1:1 blend films. (c) HOMO and LUMO levels of PFB and F8BT taken from literature.[39,40]

solvent was purchased from Sigma Aldrich (product no. 214736), degassed, and dried with 4 Å molecular sieves before use. 1:1 weight ratio PFB:F8BT solutions were made from mixing 20 mg/mL of PFB in xylenes solution and 20 mg/mL F8BT in xylenes solution. To form devices, 90 nm of PEDOT:PSS (HC Stark PEDOT 4083, lot no. LVW950) was spincoated onto an ITO substrate (Thin Film Devices, OLED/solar applications) and annealed at 120 °C under a N_2 atmosphere for 1 h. The PFB:F8BT solution was then spincoated onto the PEDOT:PSS-covered ITO in N_2 glovebox to form an 80 nm active layer. For trEFM, the film was then loaded into a flow cell with a 150 cc/min dry N_2 flow.

2.2. Photooxidation. After the PFB:F8BT blend films were made, a UV−vis spectrum was taken on one of the films to extract the absorption at each of the three degrading wavelengths of trEFM. Then, the films were exposed without top electrodes to different wavelengths, making the absorbed photon dose to be 6.0×10^{10} photons/μm^2, equal to that used in the trEFM measurements; for the in situ experiments, see below. The PFB:F8BT films were then loaded into an evaporator, and 60 nm thick Al top electrodes were deposited at 0.1 nm/s with a base pressure of 1.2×10^{-6} mbar in an Edwards 306 AUTO evaporator. EQE measurements were performed under vacuum with light from a halogen lamp dispersed by a Spectra Pro 2150i monochromator from Acton Research Corporation.

2.3. GATR-FTIR. The degradation procedures were the same as those for devices. Measurements were carried out on a Nicolet 8700 FT-IR spectrometer (Thermo Scientific) equipped with a HgCdTe detector, GATR grazing angle ATR accessory (Harrick Scientific) with a 65° fixed incident angle and a 56 in-oz slip clutch. The spectrometer and accessory were purged with dry N_2 gas. Each spectrum was taken with 256

averages. Each raw spectrum was corrected with atmospheric suppression and ATR correction; the baseline was then subtracted.

2.4. AFM. trEFM measurements were carried out on MFP-3D-BIO (Asylum Research)-based AFM with custom modifications using 300 kHz Pt-coated cantilevers (BudgetSensor ElectriTap300). trEFM was carried out in a flow cell at a lift height of 10 nm. For all trEFM data, the flow cell was connected to flowing nitrogen. The flow cell used here has a 1.50 to 2.55 mL fluid volume after engaging the tip. For photooxidation, the flow cell was connected to compressed air and exposed to light calibrated to yield an absorbed photon dose of 6.0×10^{10}/μm^2. The system was then purged again with nitrogen for another 20 min before taking the postoxidation trEFM images. The trEFM setup used is shown in Figure 2 and is described in detail elsewhere.[32,33] The 365,
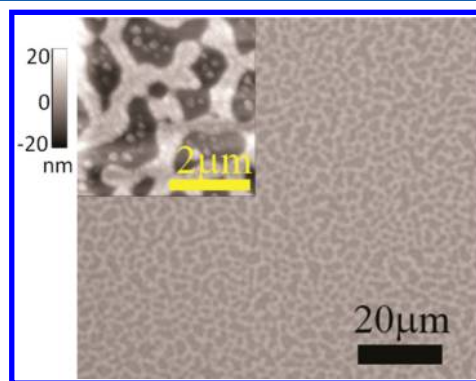

Figure 2. Photoluminescence image of a 1:1 PFB:F8BT blend. Excitation at 470 nm, emission filtered at 530 nm. Inset is the AFM topography of the same film. AFM *z*-scale bar is shown on the left.

405, and 455 nm LEDs were purchased from LED Engin (product numbers LZ1-00U600, LZ1-00UA00, LZ1-00DB00, respectively). Incident illumination power was calibrated using a Si diode and film absorbance spectra to ensure a constant absorbed photon dose at each wavelength.

3. RESULTS AND DISCUSSION

For these experiments, we chose the well-characterized model polyfluorene copolymer blend PFB:F8BT because this system provides a morphology that can be easily tailored by casting from different solvents[34,35] and because the composition of the resulting structures has been well-characterized by a range of experimental methods.[36−38]

Figure 1 shows the structures, absorption spectra, and energy levels[39,40] of PFB and F8BT as well as the optical properties of a 1:1 blend cast from xylenes. The absorbance spectra of both materials are consistent with those of classic PFB/F8BT studies,[34,35] with PFB absorbing most strongly at ~380 nm and F8BT absorbing most strongly at ~470 nm. To first order, the blend absorption appears primarily as a superposition of the two component peaks, with each material contributing roughly the same optical density at ~405 nm. The different absorption peaks of the two materials prove to be useful later because they allows us to preferentially excite each material.

Figure 2 shows a photoluminescence image of a PFB:F8BT blend film excited at 470 nm, collected with an emission filter centered at 530 nm (inset is the topography of the PFB:F8BT blend from an AFM measurement). At 530 nm, the blend emission comes predominantly from the F8BT,[34,35] and we
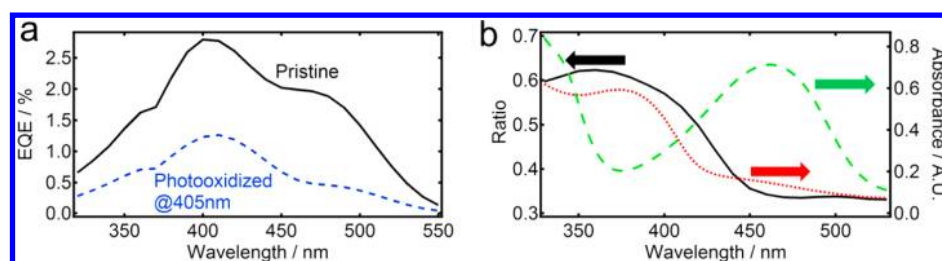
Figure 3. (a) EQE spectra of pristine and photooxidized samples. Black solid line is for pristine film. Blue dashed line is for 405 nm photooxidation. (b) The ratio of EQE versus wavelength post-/pre-photooxidation (black line), plotted on the left axis. Overlaid are the absorbance of PFB (red dotted line) and F8BT (green dashed line), respectively, plotted for reference on the right axis.

thus attribute the bright regions in the PL image (higher topography regions in the AFM image) to be F8BT-rich domains, in good agreement with previous reports of PFB/F8BT blends cast from xylenes.[34,35] The large phase separation is due to the low boiling point of the xylenes solvent being used. Such a coarse ~500 nm scale morphology is not optimal for photodiode performance but is very useful for unambiguous assignment of the domain composition and facilitates our studies of the differences in stability between different domains. Scanning-transmission X-ray microscopy (STXM) studies of similar compositions of this type of film have shown that the PFB-rich domains are ~70% PFB while F8BT-rich domains are ~90% F8BT.[38]

Figure 3a shows the external quantum efficiency (EQE) spectrum from a pristine device made from a 1:1 PFB:F8BT film of 80 nm thickness with 60 nm Al top contacts as a black trace. As expected, the PFB:F8BT combination is rather inefficient,[34,35] with a peak EQE between 2 and 3% when processed under these conditions. The pristine blend EQE trace shows features associated with the absorption spectra of both the PFB (shoulder at 405 nm) and F8BT (shoulder at 500 nm) components. Figure 3a also shows the EQE spectra from identical devices prepared on films that have been degraded in air under 405 nm illumination with absorbed photon dose of $6.0 \times 10^{10}/\mu m^2$. Importantly, the shoulder of the EQE curve beyond 450 nm (where F8BT dominates the blend absorption) degrades faster than the rest of the EQE curve, regardless of the illumination wavelength being used. Figure 3b shows this trend more clearly by plotting the ratio of device EQE before and after photooxidation. We note that after photoxidation the photocurrent response over the region from 450 to 550 nm has degraded more on a relative basis than the photocurrent response over the spectral range from 350 to 400 nm. Evidently the contribution of F8BT to the overall photocurrent decreases faster than the contribution from PFB for these samples.

We note that at these photon doses and exposure conditions the decrease in EQE cannot be from bleaching of the polymer absorption because there is no significant change in the UV−vis spectrum of the blend (see Supporting Information, Figure S1). Furthermore, there is little change even in the photoluminescence spectrum or intensity of the blend (see SI, Figure S2). Thus the loss in photocurrent is likely due to local trap formation, which changes the recombination/transport balance in the film so that even though absorption of photons is not significantly altered the successful extraction of photogenerated carriers is diminished. Because transport and recombination are highly morphology-dependent,[9] we hypothesize that any changes in transport/recombination due to photochemical degradation might also be morphology-dependent. Such a morphology dependence could arise due to many

factors ranging from composition-dependent photochemistry to morphology-dependent filamentary transport of charge carriers in the context of energetic disorder.[41,42]

To examine local variations in photooxidation with structure, we employed trEFM. Figure 4 shows an abbreviated schematic
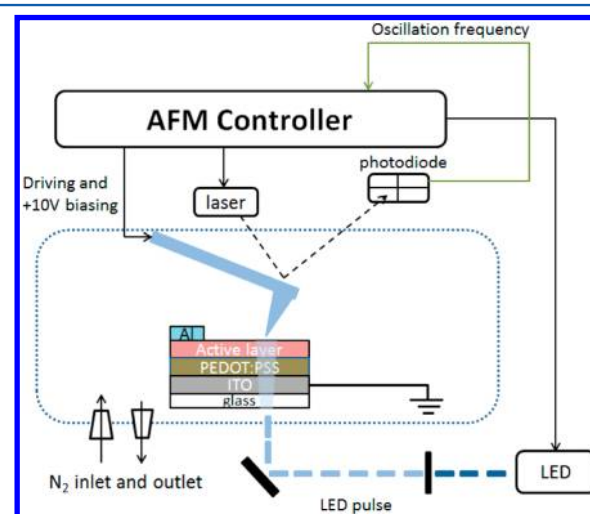

Figure 4. Schematic of trEFM setup. The sample was kept in a flow cell under a dynamic flow of dry N$_2$. The LED light was focused directly under the AFM tip to generate charges. The sample was grounded. +10 V was applied to the tip. The oscillation frequency shift of the cantilever is due to changes in the capacitance gradient that results from the changes in the distribution of charge carriers underneath the tip. The exponential decay of oscillation frequency is fitted to extract the charging rates at each point.

diagram of the trEFM apparatus that we use to measure the time rate of change of the capacitance and surface potential of a thin semiconductor film following illumination.[28,32,33] In this way, we can use trEFM as a noncontact method to measure spatial heterogeneity in local quantum efficiency due to both structural[32,33] and photochemical factors.[28] More efficient regions of the device deliver photogenerated charges to the top surface of the film at a faster rate, leading to faster charging of the tip−sample capacitor.

As depicted in Figure 4, we photodegraded films in situ using the same wavelengths (365 nm = preferential PFB excitation; 405 nm = equal PFB and F8BT excitation; and 455 nm = preferential F8BT excitation) that we used in the macroscopic photodiode experiments. In this way, we can directly image the relative changes in photocurrent arising from differences in photooxidation rates.

The top row of photooxidation in Figure 5 shows trEFM images of the same area of a pristine PFB/F8BT blend
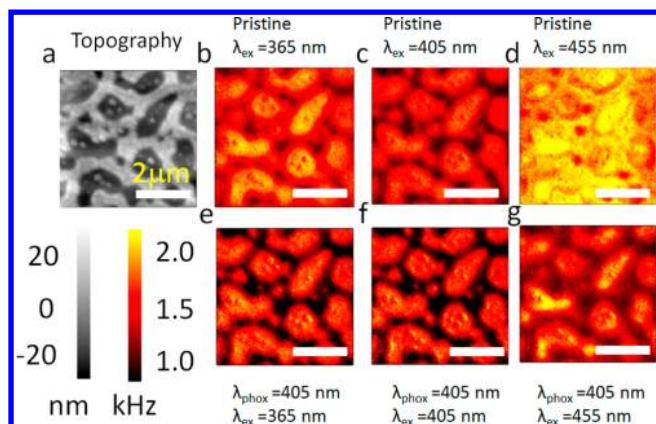
Figure 5. Charging rate maps of a given sample area. (a) Topography of the sample under investigation. (b−d) trEFM images scanned at 365, 405, and 455 nm illumination, respectively, when the sample was pristine. (e−g) trEFM images scanned at 365, 405, and 455 nm illumination, respectively, when the sample was photooxidized with 405 nm illumination.

collected with 365, 405, and 455 nm excitation sources. In each image, the bright-yellow regions correspond to faster photo-induced charging rates (more efficient local current generation and collection). The images show clear contrast, with the PFB-rich domains showing the fastest (most efficient) local rates when the film is excited at 365 or 405 nm. When the F8BT domains are preferentially excitedk, the film shows more uniform contrast but with distinct suppression of the photocurrent near the visible domain boundaries at 455 nm.

The spatial contrast in the pristine PFB:F8BT films shown in Figure 5b−d is a convolution of the compositionally induced variations in light absorption at each location and spatial variations in the quantum efficiency of the film. The local spatial variations in photocurrent collection in the PFB:F8BT system are known to be very sensitive to the exact film morphology, and undergo rapid changes in contrast near the 50:50 blend composition used in this study.[32] Here, we have used only one blend composition, and our focus is instead on exploring how image contrast evolves after photooxidation.

To photooxidize the film, we exposed it to an absorbed dose of 6.0×10^{10} photons per μm^2 from a 405 nm LED while the samples were in ambient air. We then purged the sample cell with dry nitrogen for 20 min and reimaged the samples with trEFM. Figure 5e−g shows the results, again probed with 365, 405, and 455 nm excitation. As expected, Figure 5e−g shows slower photoinduced charging rates after photooxidation, as would result from slower transport and increased recombination losses due to photochemically formed trap states.[28]

We note that Figure 5b−g also shows that the contrast between the different PFB-rich and F8BT-rich regions changes following photooxidation. Importantly, by comparing the charging rates before and after photooxidation in Figure 5, we observe faster degradation rates in the regions of higher topography (F8BT-rich domains). For instance, under 455 nm illumination, the charging rate goes from an overall almost homogeneous image (Figure 5d) to one with strong contrast (Figure 5g). Qualitatively similar results are obtained by photooxidizing at 365 or 455 nm (SI Figure S4, S5). Even when the film is degraded with 365 nm light (preferential excitation of PFB), the strongest contrast in charging rate is observed by probing with 455 nm light (preferential excitation of F8BT), with the largest loss of charging rate occurring in the F8BT-rich

regions. In other words, the trEFM data show that the F8BT-rich domains lose their ability to generate/harvest photocurrent faster than the PFB-rich domains. To better visualize the changes in trEFM charging contrast due to photooxidation, we plot the trEFM data as retained charging rate ratio images. We define the retained charging rate at each pixel as:

$$R_{CR} = \frac{k_{phox}}{k_{pristine}} \qquad (1)$$

where k_{phox} is the retained charging rate after photooxidation and $k_{pristine}$ is the charging rate on the fresh film without photooxidation. Each sample area was imaged before and after photooxidation at a single degrading wavelength, with the three probing wavelengths (365, 405, and 455 nm).

Figure 6 shows a 3×3 matrix of such retained charging rate (R_{CR}) images along with the associated film topography. The
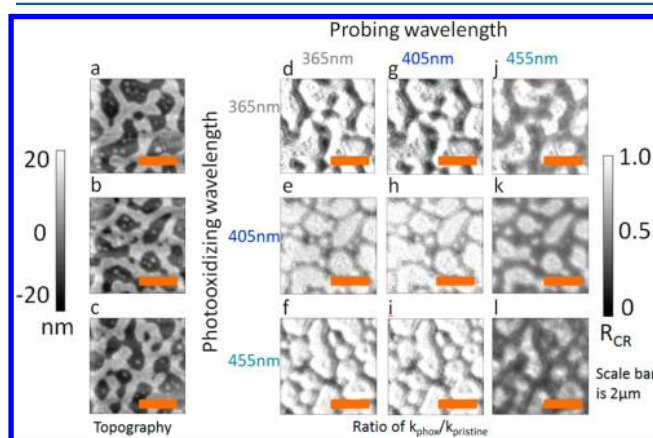

Figure 6. Charging ratio images of given areas. For each row, the image on the left-hand side is the topography of area under investigation. (a) for d, g, and j; (b) for e, h, and k; and (c) for f, i, and l. For the 3×3 block on the right, each one is the charging ratio image before and after photooxidation. For example, each pixel in panel e is the charging rate ratio probed with 365 nm illumination before and after photooxidation with 405 nm illumination. All of the charging rate ratio images share the same scale bar on the right. The average value of charging rate is lower when probing with 455 nm illumination.

data shown correspond to 21 total scans and 3 separate photooxidations. Bright areas are those that show little degradation after air/light exposure while dark areas are those that show significant degradation. These images provide dramatic visual evidence of our contention that the F8BT-rich regions of the film are losing their photocarrier generation/collection efficiency faster than the PFB-rich domains. Figure 6d−l shows that regardless of what wavelength is used to photooxidize the film and no matter what wavelength is used to photoexcite the film during for trEFM measurement the result is always the same: the F8BT-rich domains are darker in the ratio images, indicating they retained a smaller fraction of their initial efficiency after photooxidation. The images are all displayed with the same z-axis color scale. We do observe a greater extent of photooxidation in Figure 6j−l, all probed with 455 nm, perhaps because this wavelength is preferentially absorbed by F8BT.

Qualitatively, Figure 6 shows clearly that for all excitation wavelengths the F8BT-rich domains are losing their ability to generate photocurrent more rapidly than the PFB-rich

domains. A quantitative analysis (SI Table S1) shows that the degradation of the F8BT-rich domains is anywhere from 1.1 to 2.5 times faster than the PFB-rich domains depending on the degradation and probing wavelengths used. On the upper end, these ratios (SI Table S1) are just outside the ratio of F8BT concentration present in these domains, and one might thus interpret our data as indicating that degradation is simply linearly proportional to local F8BT concentration within a domain. However, an examination of the wavelength-dependent data in Figure 6 (and the ratios at different wavelengths, SI Table S1) shows that at wavelengths where only F8BT absorbs the response of the F8BT within the F8BT-rich regions is falling off *faster* than the response of the F8BT within the PFB-rich regions.

The trEFM photooxidation data are not only consistent with the device data but thus add a suggestive level of missing detail. Indeed, the trEFM data suggest that the reason that the F8BT photoresponse shown in Figure 3 is falling off faster in the macroscopic photodiode measurements is because the regions where most of the F8BT absorption is taking place (the F8BT-rich domains) suffer from faster relative photooxidation overall.

These images provide important evidence in support of the hypothesis that local film structure will affect the local stability of the blend during photovoltaic operation. The origin of this local variation is a matter for speculation. It seems troubling that the F8BT-rich regions would lose performance fastest, as we would generally expect F8BT to be more oxidatively stable than PFB due to its greater ionization potential (Figure 1).[39,40] Indeed, when we subjected neat films of PFB and F8BT to photooxidation experiments characterized by grazing angle attenuated total reflection GATR-FTIR, we found that at the same dosage PFB degrades much faster than F8BT, evidenced by the dramatic difference in keto-defect peak ~1720 cm^{-1}, Figure 7. This is the carbonyl stretch of fluorenone.[28,43] Keto-
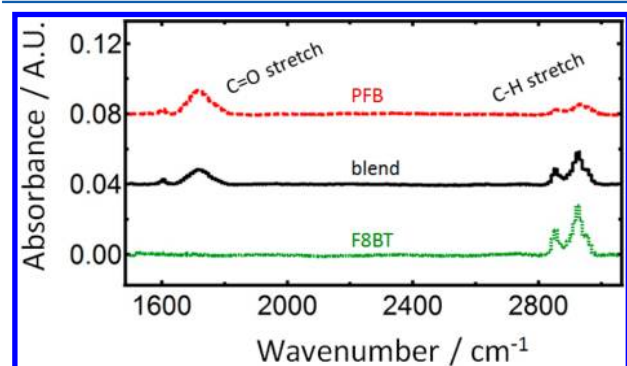

Figure 7. GATR-FTIR absorbance spectrum of PFB, blend, and F8BT after photooxidation with absorbed photon dose of $2.0 \times 10^{12}/\mu m2$ with 405 nm LED. Ketone defect formation is indicated by C=O stretch ~1720 cm^{-1}.

defects have been found to be electron trapping.[44] However, we point out that the photochemical reaction is a complex process that yields a variety of products. Their respective charge-transport properties are not well-investigated, and blends undergoing photoinduced charge transfer may react differently than pristine materials.

In PFB/F8BT-based OLEDs it has been reported that dedoping of the PEDOT:PSS layers as a result of pinhole defects in the electrode could explain performance losses over time.[45] However, we do not believe that such a mechanism can

explain our photodegradation data because the current density should be higher in the PFB-rich domains and lower in the F8BT-rich domains, thus, if the loss of device performance was from dedoping of the underlying PEDOT:PSS layer, then we should expect the PFB-rich domains to degrade faster, which is the opposite of what we observe.

Given these contradictions and the evidence for lower oxidative stability of our PFB relative to our F8BT samples, we speculate that the origin of the spatial variation in stability observed in Figures 5 and 6 could be due to the breakdown of nanoscopic PFB hole transport pathways in the blend. Ironically then, our working hypothesis would suggest that the F8BT-rich domains are degrading fastest because they have a lower fraction of less stable PFB (typically ~10%,[38] the exact composition may depend on the microscopic location, processing conditions such as spin-coating speed, and temperature, but there is no doubt of dominance of F8BT in the F8BT-rich domains,[36−38] making the few PFB-based hole-transport pathways that exist in those domains more susceptible to low levels of damage).

To test this hypothesis, we used conductive AFM (cAFM) to measure the hole current through the film injected by a gold tip. Because of the better alignment of the HOMO level of PFB with gold,[39,40] hole current is predominantly carried by the PFB component in both phases in the blend, which is confirmed by Figure 8b because there is a larger PFB composition in the
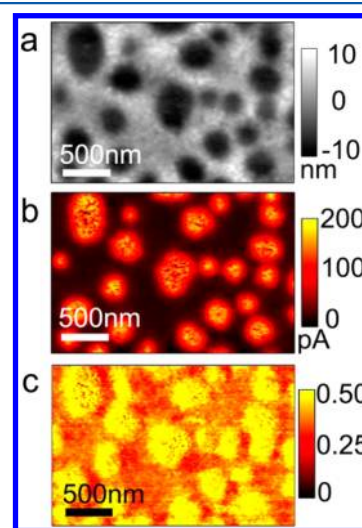

Figure 8. Current image of a PFB:F8BT blend after photooxidation. (a) Topography image of the sample area. (b) Current image of pristine sample under 5 V bias. (c) Retained current ratio image plotting the ratio of injected hold current before and after photooxidation, showing that whereas the PFB-rich domains have much higher hole injection current densities, in both cases, the F8BT-rich domains show the biggest proportional decrease in hole current following photooxidation.

lower topography, PFB-rich regions.[36−38] After photooxidation with 405 nm at the photon dose used in trEFM, we observe a larger loss of hole current in the F8BT-rich phases shown in Figure 8c. Figure 8c is a hole current ratio image, defined as hole current post-/pre-photooxidation. Each pixel in the image is of the value:

$$R_{current} = \frac{I_{phox}}{I_{pristine}} \qquad (2)$$

where $I_{pristine}$ is the current before photooxidation and I_{phox} is the current of the same pixel after photooxidation. The current ratio image suggests that proportionally hole current loss is higher in the F8BT-rich domain than in the PFB-rich domain. If photooxidation was merely doping the polymer, then we would expect a rise in the hole current.[24,46] However, we see a drop of current over the entire image. This drop would be consistent with a breakdown of hole transport pathways due to photooxidation and we therefore conclude that our cAFM data are consistent with our hypothesis that the loss of photocurrent in the F8BT-rich domains could be from the degradation of hole transport pathways. However, we point out that this hypothesis will still need to be tested further and hope our findings will stimulate future experimentation.

4. CONCLUSIONS

We have used a combined study of trEFM and device EQE measurements to show that the rate of device aging in nanostructured polymer solar cells can depend on local composition in a model polyfluorene copolymer blend solar cell. After photooxidizing the films, we observed that the device EQE spectra show a reduced contribution from the spectral region attributable to F8BT absorption. Importantly, the in situ trEFM data show that this result can be explained by a relatively faster decay of the photocurrent contributions from the F8BT-rich domains to the net device photocurrent, even while the F8BT present in PFB-rich domains appears to continue to contribute to the device photocurrent. Consistent with our FTIR and cAFM data, we speculate that this differential degradation could be the result of broken percolation networks of the minority PFB chains within the F8BT-rich networks. Overall, these data show that local compositional heterogeneity can affect device aging and that an understanding of photochemical degradation and trap formation on the nanoscale could prove to be invaluable in understanding and improving the lifetime performance of organic solar cells.

ASSOCIATED CONTENT

Ⓢ Supporting Information

Additional notes on UV–vis absorbance and photoluminescence spectrum pre-/post-photooxidation, lack of degradation of the films during imaging, charging rates probed with different wavelengths after photooxidation with 365 and 455 nm illumination, degradation versus time data, and quantitative values for the ratio of the R_{CR} plots computed separately for PFB-rich and F8BT-rich domains. This material is available free of charge via the Internet at http://pubs.acs.org

AUTHOR INFORMATION

Corresponding Author

*E-mail: ginger@chem.washington.edu.

Notes

The authors declare no competing financial interest.

ACKNOWLEDGMENTS

REFERENCES

(1) Halls, J. J. M.; Walsh, C. A.; Greenham, N. C.; Marseglia, E. A.; Friend, R. H.; Moratti, S. C.; Holmes, A. B. Nature 1995, 376, 498–500.
(2) Yu, G.; Gao, J.; Hummelen, J. C.; Wudl, F.; Heeger, A. J. Science 1995, 270, 1789–1791.
(3) http://www.polyera.com/newsflash/polyera-achieves-world-record-organic-solar-cell-performance (accessed Jan 13, 2013).
(4) http://www.heliatek.com/newscenter/latest_news/heliatek-erzielt-mit-107-effizienz-neuen-weltrekord-fur-seine-organische-tandemzelle/?lang=en (accessed Jan 13, 2013).
(5) http://newsroom.ucla.edu/portal/ucla/ucla-engineers-create-tandem-polymer-228468.aspx (accessed Jan 13, 2013).
(6) Coakley, K. M.; McGehee, M. D. Chem. Mater. 2004, 16, 4533–4542.
(7) Kippelen, B.; Bredas, J. L. Energy Environ. Sci. 2009, 2, 251–261.
(8) Krebs, F. C.; Gevorgyan, S. A.; Alstrup, J. J. Mater. Chem. 2009, 19, 5442–5451.
(9) Groves, C.; Reid, O. G.; Ginger, D. S. Acc. Chem. Res. 2010, 43, 612–620.
(10) Jorgensen, M.; Norrman, K.; Krebs, F. C. Sol. Energy Mater. Sol. Cells 2008, 92, 686–714.
(11) Reese, M. O.; Nardes, A. M.; Rupert, B. L.; Larsen, R. E.; Olson, D. C.; Lloyd, M. T.; Shaheen, S. E.; Ginley, D. S.; Rumbles, G.; Kopidakis, N. Adv. Funct. Mater. 2010, 20, 3476–3483.
(12) Reese, M. O.; Morfa, A. J.; White, M. S.; Kopidakis, N.; Shaheen, S. E.; Rumbles, G.; Ginley, D. S. Sol. Energy Mater. Sol. Cells 2008, 92, 746–752.
(13) Yang, X. N.; van Duren, J. K. J.; Janssen, R. A. J.; Michels, M. A. J.; Loos, J. Macromolecules 2004, 37, 2151–2158.
(14) Seemann, A.; Sauermann, T.; Lungenschmied, C.; Armbruster, O.; Bauer, S.; Egelhaaf, H. J.; Hauch, J. J. Sol. Energy 2011, 85, 1238–1249.
(15) Chen, L.-M.; Hong, Z.; Li, G.; Yang, Y. Adv. Mater. 2009, 21, 1434–1449.
(16) Hau, S. K.; Yip, H.-L.; Baek, N. S.; Zou, J.; O'Malley, K.; Jen, A. K. Y. Appl. Phys. Lett. 2008, 92, 2533011–2533013.
(17) Drees, M.; Hoppe, H.; Winder, C.; Neugebauer, H.; Sariciftci, N. S.; Schwinger, W.; Schaffler, F.; Topf, C.; Scharber, M. C.; Zhu, Z.; et al. J. Mater. Chem. 2005, 15, 5158–5163.
(18) Krebs, F. C.; Spanggaard, H. Chem. Mater. 2005, 17, 5235–5237.
(19) Kim, B. J.; Miyamoto, Y.; Ma, B.; Frechet, J. M. J. Adv. Funct. Mater. 2009, 19, 2273–2281.
(20) Krebs, F. C.; Norrman, K. Prog. Photovoltaics 2007, 15, 697–712.
(21) Bässler, H.; Schonherr, G.; Abkowitz, M.; Pai, D. M. Phys. Rev. B 1982, 26, 3105–3113.
(22) Pasveer, W. F.; Cottaar, J.; Tanase, C.; Coehoorn, R.; Bobbert, P. A.; Blom, P. W. M.; de Leeuw, D. M.; Michels, M. A. J. Phys. Rev. Lett. 2005, 94, 2066011–2066014.
(23) Zhuo, J.-M.; Zhao, L.-H.; Png, R.-Q.; Wong, L.-Y.; Chia, P.-J.; Tang, J.-C.; Sivaramakrishnan, S.; Zhou, M.; Ou, E. C. W.; Chua, S.-J.; et al. Adv. Mater. 2009, 21, 4747–4752.
(24) Abdou, M. S. A.; Orfino, F. P.; Son, Y.; Holdcroft, S. J. Am. Chem. Soc. 1997, 119, 4518–4524.
(25) Coffey, D. C.; Reid, O. G.; Rodovsky, D. B.; Bartholomew, G. P.; Ginger, D. S. Nano Lett. 2007, 7, 738–744.
(26) Pingree, L. S. C.; Reid, O. G.; Ginger, D. S. Adv. Mater. 2009, 21, 19–28.
(27) Giridharagopal, R.; Ginger, D. S. J. Phys. Chem. Lett. 2010, 1, 1160–1169.
(28) Reid, O. G.; Rayermann, G. E.; Coffey, D. C.; Ginger, D. S. J. Phys. Chem. C 2010, 114, 20672–20677.
(29) Balke, N.; Bonnell, D.; Ginger, D. S.; Kemerink, M. MRS Bull. 2012, 37, 633–637.
(30) O'Dea, J. R.; Brown, L. M.; Hoepker, N.; Marohn, J. A.; Sadewasser, S. MRS Bull. 2012, 37, 642–650.

4659

dx.doi.org/10.1021/jp3090843 | J. Phys. Chem. B 2013, 117, 4654–4660

(31) Sengupta, E.; Domanski, A. L.; Weber, S. A. L.; Untch, M. B.; Butt, H.-J. r.; Sauermann, T.; Egelhaaf, H. J.; Berger, R. D. *J. Phys. Chem. C* **2011**, *115*, 19994−20001.

(32) Coffey, D. C.; Ginger, D. S. *Nat. Mater.* **2006**, *5*, 735−740.

(33) Giridharagopal, R.; Rayermann, G. E.; Shao, G.; Moore, D. T.; Reid, O. G.; Tillack, A. F.; Masiello, D. J.; Ginger, D. S. *Nano Lett.* **2012**, *12*, 893−898.

(34) Arias, A. C.; MacKenzie, J. D.; Stevenson, R.; Halls, J. J. M.; Inbasekaran, M.; Woo, E. P.; Richards, D.; Friend, R. H. *Macromolecules* **2001**, *34*, 6005−6013.

(35) Snaith, H. J.; Arias, A. C.; Morteani, A. C.; Silva, C.; Friend, R. H. *Nano Lett.* **2002**, *2*, 1353−1357.

(36) Stevenson, R.; Arias, A. C.; Ramsdale, C.; MacKenzie, J. D.; Richards, D. *Appl. Phys. Lett.* **2001**, *79*, 2178−2180.

(37) Brenner, T. J. K.; McNeill, C. R. *J. Phys. Chem. C* **2011**, *115*, 19364−19370.

(38) McNeill, C. R.; Watts, B.; Thomsen, L.; Ade, H.; Greenham, N. C.; Dastoor, P. C. *Macromolecules* **2007**, *40*, 3263−3270.

(39) Moons, E. *J. Phys.: Condens. Matter* **2002**, *14*, 12235−12260.

(40) Morteani, A. C.; Dhoot, A. S.; Kim, J. S.; Silva, C.; Greenham, N. C.; Murphy, C.; Moons, E.; Cina, S.; Burroughes, J. H.; Friend, R. H. *Adv. Mater.* **2003**, *15*, 1708−1712.

(41) Tessler, N.; Preezant, Y.; Rappaport, N.; Roichman, Y. *Adv. Mater.* **2009**, *21*, 2741−2761.

(42) Coehoorn, R.; Pasveer, W. F.; Bobbert, P. A.; Michels, M. A. J. *Phys. Rev. B* **2005**, *72*, 1522061−15220620.

(43) Liu, L. L.; Tang, S.; Liu, M. R.; Xie, Z. Q.; Zhang, W.; Lu, P.; Hanif, M.; Ma, Y. G. *J. Phys. Chem. B* **2006**, *110*, 13734−13740.

(44) Yang, X. H.; Jaiser, F.; Neher, D.; Lawson, P. V.; Bredas, J. L.; Zojer, E.; Guntner, R.; de Freitas, P. S.; Forster, M.; Scherf, U. *Adv. Funct. Mater.* **2004**, *14*, 1097−1104.

(45) Kim, J. S.; Ho, P. K. H.; Murphy, C. E.; Baynes, N.; Friend, R. H. *Adv. Mater.* **2002**, *14*, 206−209.

(46) Meijer, E. J.; Detcheverry, C.; Baesjou, P. J.; van Veenendaal, E.; de Leeuw, D. M.; Klapwijk, T. M. *J. Appl. Phys.* **2003**, *93*, 4831−4835.